Modelling the effect of concrete cement composition on its strength and failure behavior

Timo Saksala[1], Kari Kolari and Reijo Kouhia

Summary   Typical concrete is a mixture of Portland cement, water, and aggregates. While aggregates have a substantial effect on the concrete strength and fracture behavior, the focus of the present study is on the hardened cement paste which can be further divided into the unreacted core, inner and outer products. In high strength concrete, water-to-cement ratio is low, and thus the distance between cement particles is small. Also, the amount of unreacted (high strength) core is higher, and the porosity is low. When water-to-cement ratio is higher, both the distance between cement particles and the porosity due to capillary pores increases. In the present study, we develop a numerical model based on the embedded discontinuity finite elements to predict the effect of the water-to-cement ratio on the compressive fracture behavior of concrete. Representative 2D plane strain simulations demonstrate that the present method captures the major features of concrete fracture and, particularly, qualitatively predicts the known effects of the water-to-cement ratio on concrete compressive strength.

Key words: concrete fracture, cement-to-water ratio, mesoscopic modelling, embedded discontinuities, finite elements

Introduction

Concrete is the most widely used building material of the world. From the structural engineering point of view, it is thus crucial to understand the effects of the typical concrete constituents, i.e., Portland cement (~20 wt%), water (~10 wt%), and aggregates (~70 wt%), on its strength and fracture behavior. When concrete is cast into a mold, a hydration process of cement starts, forming mainly Calsium Silicate Hydrate (C-S-H) which binds the aggregates together and gives the concrete its strength. The hardened cement paste can further be divided into the unreacted core (of a cement particle), inner and outer products.

---

[1]Corresponding author: timo.saksala@tuni.fi

The water-to-cement ratio has also a substantial effect on the concrete strength. In high strength concrete, water-to-cement ratio is low [1], and thus the distance between the cement particles is small. Also, the amount of unreacted (high strength) cores is higher, and the porosity is low. When water-to-cement ratio is higher, both the distance between cement particles and the porosity due to capillary pores increases [1]. These concepts are schematically illustrated in Figure 1, showing also an electron microscope image of the main hydration product C-S-H.
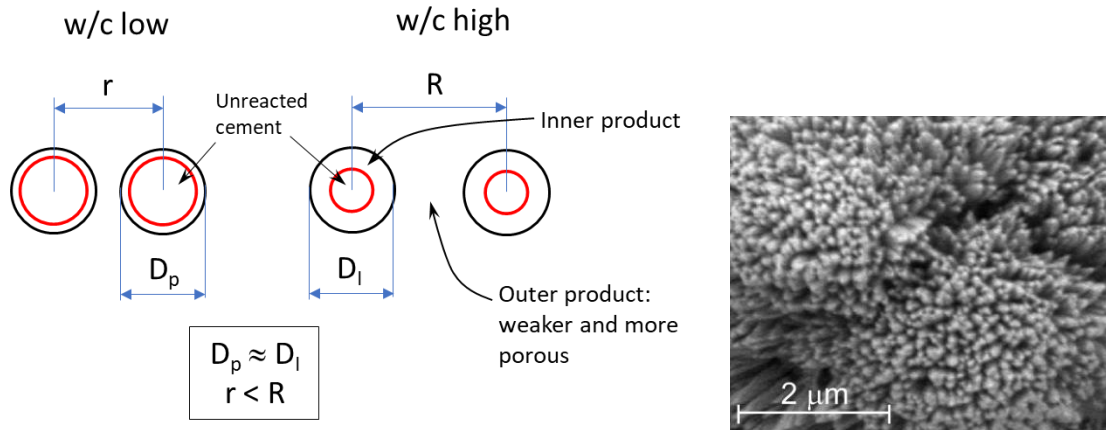

Figure 1. Schematic illustration of hardened cement paste with low and high water-to-cement ratio (left), and electron microscope image of C-S-H (right, figure by VTT).

Naturally, concrete is also one of the most studied material, both experimentally [2] and numerically [3]. At the structural scale, the numerical modelling of concrete structures is typically based on macroscale damage/plasticity constitutive models implemented in the finite element method (FEM) [4–6]. This approach, appropriate especially in the analysis of massive structures, homogenizes the bi-phasic mesostructure of concrete. At the representative volume element scale, a mesoscopic approach describing explicitly the concrete mesostructure, i.e., the hardened cement matrix and the aggregates, is often adopted [7–10]. However, modelling the effect of water-to-cement ratio on concrete strength seems rare.

In this paper, we develop a numerical model to predict the effect of the water-to-cement ratio on the fracture behavior of concrete under uniaxial tension and compression. At this stage of developments, the effect of aggregates is neglected due to the different length scales of aggregates (usually visible to the naked eye) and cement particles (usually not visible to the naked eye). Moreover, we assume that the three sub-phases of the hardened cement paste can be represented, for purely mechanical purposes, as a linear elastic fracturing material, where the fracture is described by the embedded discontinuity finite elements. This method is chosen as it is an enriched finite element method being thus superior in fracture description over the classical FEM based on the smeared damage-plasticity description of material failure. Moreover, the reason for choosing the embedded discontinuity FEM approach instead of the extended FEM is the fully local nature of the former. This allows static condensation of the extra degrees of freedom representing the discontinuity jumps in quasi-static and implicit dynamic analyses. In the explicit setting,

the fully local nature allows to implement the discontinuity kinematics and the traction-separation law analogous to plasticity models, which means that the robust local return mapping algorithms can be readily used. The model originally developed by Saksala [11] is adopted here. Representative 2D plane strain numerical simulations demonstrate that the present method captures the major features of concrete fracture both under tension and compression and, particularly, qualitatively predicts the known effects of the water-to-cement ratio on concrete strength. The 2D plane strain assumption is chosen for simpler implementation and computational economy reasons.

Numerical method

Concrete fracture model

Fracturing of the hardened cement paste is modelled by the embedded discontinuity approach. This method describes a crack by a displacement discontinuity embedded inside a finite element [12]. In the multiple discontinuity version, many intersecting discontinuities can be embedded inside an element. The present study employs the constant strain triangle (CST) element with three embedded discontinuities (see Figure 2). For this element, the displacement and strain fields can be written as [11,13]

$$\mathbf{u}(\mathbf{x}) = N_i(\mathbf{x})\mathbf{u}_i^e + \sum_{k=1}^{3} M_{\Gamma_d}^k(\mathbf{x})\, \boldsymbol{\alpha}_d^k \quad \text{with} \quad M_{\Gamma_d}^k(\mathbf{x}) = H_{\Gamma_d}^k(\mathbf{x}) - \varphi_k(\mathbf{x}) \tag{1}$$

$$\boldsymbol{\varepsilon}(\mathbf{x}) = (\nabla N_i \otimes \mathbf{u}_i^e)^{sym} - \sum_{k=1}^{3}\left(\left(\nabla\varphi_k(\mathbf{x}) \otimes \boldsymbol{\alpha}_d^k\right)^{sym} + \delta_{\Gamma_d}^k\left(\mathbf{n}_k \otimes \boldsymbol{\alpha}_d^k\right)^{sym}\right) \tag{2}$$

where N_i and $\mathbf{u}_i^e$ are the standard interpolation functions and nodal displacements ($i = 1,2,3$ with summation on repeated indices), respectively, and the displacement jump at each discontinuity is denoted by $\boldsymbol{\alpha}_d^k$. In addition, $H_{\Gamma_d}^k$ and $\delta_{\Gamma_d}^k$ are the Heaviside function and its gradient, the Dirac delta function. The usual (with low order elements) elementwise constant displacement jump assumption, yielding $\nabla\boldsymbol{\alpha}_d^k \equiv \mathbf{0}$, was exploited in arriving at the expression (2).

The reason for using the awkward decomposition (1), instead of the intuitive one with $\varphi_k \equiv 0$, is that this one restricts the effect of $\boldsymbol{\alpha}_d^k$ inside the corresponding finite element making the formulation fully local, i.e., $\boldsymbol{\alpha}_d^k \equiv \mathbf{0}$ outside that element. Thereby, the embedded discontinuity enrichment does not increase the global degrees of freedom.

Functions φ_k appearing in $M_{\Gamma_d}^k$ need to be specified. For elements with three intersecting discontinuities parallel to the element edges (see Figure 2), these functions are simply the shape functions of the opposite nodes, i.e., $\varphi_k = N_k$. The crack normals are thus $\mathbf{n}_i = \nabla N_i / \|N_i\|$. If the element has only a single discontinuity, φ is chosen, from among the possible combinations of the shape functions, so that its gradient is as parallel as possible to the crack normal $\mathbf{n}_d$:

$$\nabla\varphi = \arg\left(\max_{k=1,2} \frac{\left|\sum_{i=1}^{k}\nabla N_i \cdot \mathbf{n}_d\right|}{\left\|\sum_{i=1}^{k}\nabla N_i\right\|}\right) \tag{3}$$

Following [10,14], the enhanced assumed strains (EAS) concept is used to impose the traction continuity over the discontinuities. This means that the variation of the enhanced

part of the strain in (1) is constructed in the strain space orthogonal to the stress field (details are in [10,14]). With the CST element, the strong (local) form of traction continuity finally reads

$$\mathbf{t}_{\Gamma_d}^i = \boldsymbol{\sigma} \cdot \mathbf{n}_i = \left(\mathbf{E} \colon \left(\hat{\boldsymbol{\varepsilon}} - \sum_{k=1}^3 \left(\nabla N_k(\mathbf{x}) \otimes \boldsymbol{\alpha}_d^k \right)^{sym} \right) \right) \cdot \mathbf{n}_i \qquad (4)$$

where $\mathbf{n}_i$ is the crack (discontinuity) normal, $\hat{\boldsymbol{\varepsilon}} = (\nabla N_i \otimes \mathbf{u}_i^e)^{sym}$, $\mathbf{E}$ is the elasticity tensor, and $\boldsymbol{\sigma}$ and $\boldsymbol{\varepsilon}$ are the stress and (total) strain tensor, respectively. This formulation results in a simple implementation that requires neither the explicit position of the discontinuity within the element nor its length to be known.
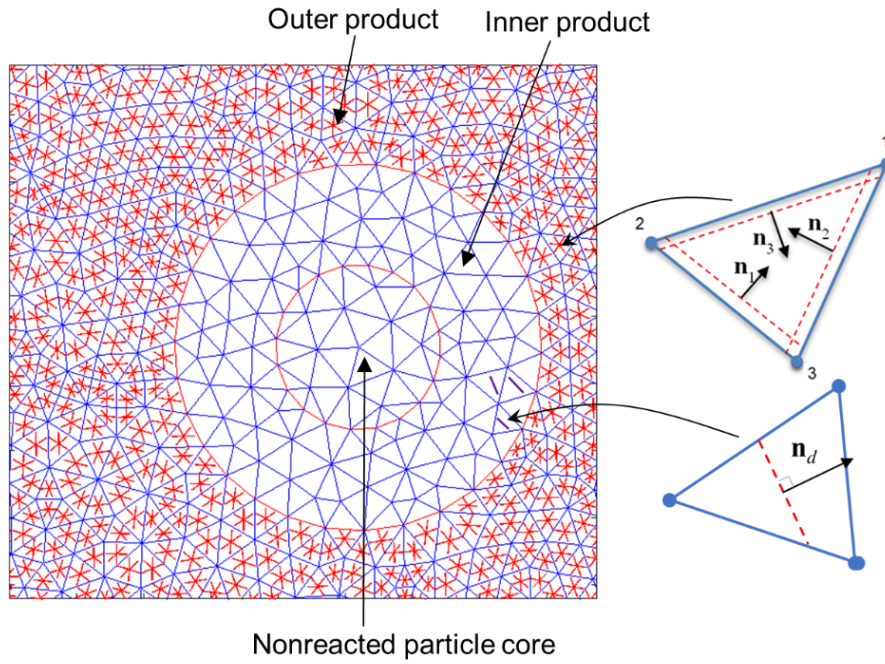

Figure 2. Numerical representation (finite element mesh) of the hardened cement paste and the fracture types.

Next, the concepts presented above are applied to fracturing hardened cement paste, as illustrated in Figure 2. An idealized geometry of concentric circles is assumed for the presentation of the cement particles and the inner product layer around them. The unreacted core and the inner reaction product, modelled as a strip of finite elements surrounding the core, fail according to the first principal stress criterion. Upon its violation, a discontinuity (crack) with a normal parallel to the first principal direction is introduced in a finite element during analysis. The third phase represents both the outer hydration product and the capillary space between cement particles. Therefore, the strength of the third phase decreases with increasing water-to-cement ratio. However, this feature is neglected here. The failure of the "hairy-like" outer reaction products is described by pre-embedded discontinuities, three in each triangular element in the mesh, aligned parallel to the element edges (Figure 2).

Traction-separation model for solving the crack opening

A method for solving the displacement jump increments and the traction-separation law at each discontinuity is needed. For this end, a computational multisurface plasticity inspired model based on the classical elastic predictor-plastic corrector split is employed. The relevant model components, i.e., the loading functions ϕ_i, softening rules and evolution laws are defined as

$$\phi_i\left(\mathbf{t}_{\Gamma_d}^i, \kappa_i, \dot{\kappa}_i\right) = \mathbf{n}_i \cdot \mathbf{t}_{\Gamma_d}^i + \beta\left|\mathbf{m}_i \cdot \mathbf{t}_{\Gamma_d}^i\right| - \left(\sigma_t + q_i(\kappa_i, \dot{\kappa}_i)\right) \tag{5}$$

$$q_i = h_i \kappa_i + s \dot{\kappa}_i, \quad h_i = -g \sigma_t \exp(-g \kappa_i), \quad g = \frac{G_{Ic}}{\sigma_t} \tag{6}$$

$$\dot{\mathbf{t}}_{\Gamma_d}^i = -\mathbf{E} : \sum_{k=1}^{3}\left(\nabla N_k(\mathbf{x}) \otimes \dot{\boldsymbol{\alpha}}_d^k\right)^{sym} \cdot \mathbf{n}_i \tag{7}$$

$$\dot{\boldsymbol{\alpha}}_d^i = \dot{\lambda}_i \frac{\partial \phi_i}{\partial \mathbf{t}_{\Gamma_d}^i}, \quad \dot{\kappa}_i = -\dot{\lambda}_i \frac{\partial \phi_i}{\partial q_i} \tag{8}$$

$$\dot{\lambda}_i \geq 0, \quad \phi_i \leq 0, \quad \dot{\lambda}_i \phi_i = 0 \quad (i, j = 1,2,3) \tag{9}$$

where $\mathbf{m}_i$ denotes the unit tangent of a discontinuity, $\kappa_i, \dot{\kappa}_i$ are the internal variable and its rate related to the softening law for a discontinuity, and σ_t and s are the tensile strength and the viscosity of the material. Moreover, h_i is the softening modulus of the exponential softening rule. By (8), the internal variable is identical with the viscoplastic multiplier, i.e., $\dot{\kappa}_i \equiv \dot{\lambda}_i$. Parameter g controls the initial slope of the softening curve and is calibrated by the mode I fracture energy G_{Ic}. Finally, β is a parameter that controls the effect of shear (mode-II) component of the traction. The material behaviour is isotropic and linearly elastic until the tensile strength is reached. The equations (9) are the classical Kuhn–Tucker conditions that impose the consistency.

As the model described by Equations (5)–(9) is analogous to viscoplastic consistency model by Wang et al. [16], it can be solved by the standard methods of computational plasticity. That is, a trial stress is first calculated based on Equation (5) where the present total strain comes from the global solution. Then, the trial values (evaluated with the trial stress) of the loading functions in (5) are checked. If violated, an inelastic corrector step, i.e., the integration of the equations in (6)–(8), is performed and the new values for internal variables and the displacement jump are obtained. Then, the new stress is calculated based on Equation (5) after which the internal force vector for each element is computed.

Numerical examples

Material and model parameters, and the numerical concrete samples

Material and model parameters used in the present 2D plane strain simulations are given in Table 1. The values are for demonstrational purposes only and may not thus be realistic ones for the three subphases of the hardened cement paste. It should be reminded that it is challenging, if not impossible, to measure the elastic and strength properties of these three subphases. However, intuitively the unreacted core should be the strongest and the outer product weakest. The tensile strength values in Table 1 reflect this order. Moreover, the outer product tensile strength and Young's modulus are typical for Portland cement.

Table 1. Material properties for simulations.

Property/Mineral	Unreacted core	Inner product	Outer product
E [GPa]	60	27.5	27.5
ν	0.2	0.2	0.2
σ_{t0} [MPa]	10	6	3.5
G_{Ic} [N/m]	0.04	0.02	0.02
ρ [kg/m^3]	2400	2400	2400
s [MPa·s/m]	0.001	0.001	0.001
β	1	1	1

Figure 3 shows the numerical concrete samples, and the finite element meshes. The first sample (Conc1, with 30 cement particles) represents the cement paste with higher w/c ratio, while the second (Conc2, with 60 cement particles) has lower w/c ratio, corresponding to the idealized features in Figure 1.

It should be noted that the dimensions of the samples are highly exaggerated for computational economy reasons and do not represent the true scale of unreacted cement particles having a diameter in the range of 1−100 μm. Some numerical values characterizing the numerical concrete samples are calculated in Table 2, where A_{uc}, A_{ip}, A_{op}, A_{tot} are the areas of the unreacted cores, inner products, outer products, and the total sample areas, respectively.

Table 2. Characteristics of the numerical concrete models.

Sample/fraction	A_{uc}/A_{tot}	A_{ip}/A_{tot}	A_{op}/A_{tot}
Conc1	0.054	0.211	0.735
Conc2	0.287	0.229	0.490

The global equations of motion are solved explicitly in time with a self-written Matlab code. This choice requires, due to the critical time step, using rather high loading rate to carry out uniaxial tests on the samples in Figure 3. For this reason, the viscosity moduli in Table 1 are chosen small enough not to cause any strain rate hardening effects.
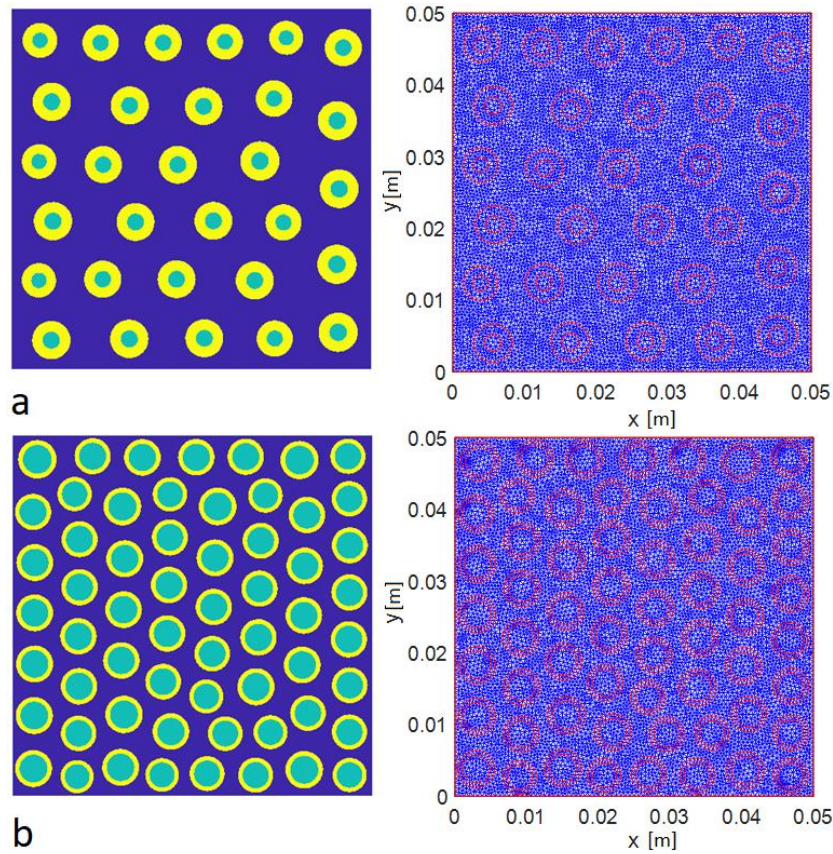
Figure 3. Numerically modelled concrete (Conc1) and the FE mesh (21431 elements) (a), and numerically modelled concrete 2 (Conc2) and the FE mesh (20350 elements) (b).

Uniaxial tension test

Uniaxial tension test on the numerical concrete samples is carried out here. The samples are simply supported at the lower edge, while a constant velocity boundary condition (BC) is applied at the upper edge with $v_0 = 0.01$ m/s resulting in an average strain rate of 0.2 s^{-1}. The simulation results are shown in Figure 4.

The predicted failure modes for both numerical samples attest the experimental transversal splitting of the sample with some local differences. However, the predicted tensile strengths, 3.048 MPa for Conc1 (higher w/c ratio) and 3.085 MPa for Conc2 (lower w/c ratio), are almost the same, i.e., the model does not predict the weakening effect of increasing water content. The reason for this is clearly the strength of the third, outer products, phase is assumed constant when it should decrease with increasing water-to-cement ratio.
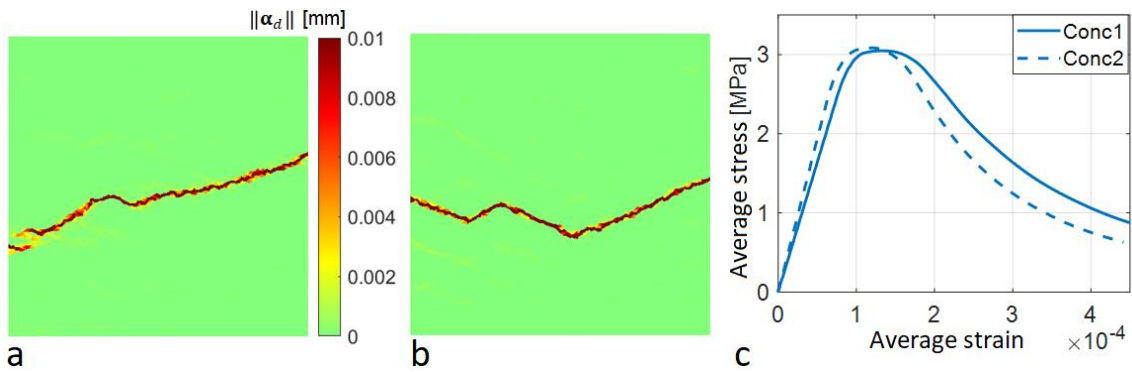
61

Figure 4. Simulation results for uniaxial tension test: Failure mode (in terms of crack opening magnitude) numerical concrete (Conc1) (a), numerical concrete 2 (Conc2) (b), and the corresponding stress-strain curves c).

Uniaxial compression test

Uniaxial compression test on the numerical concrete samples is carried out here. As with the uniaxial tension test, lower edge is simply supported, and a constant velocity BC is applied at the upper edge with $v_0 = 0.05$ m/s resulting in a strain rate of 1 s^{-1} (higher loading rate is used in compression since the compressive strength is roughly 10 times higher for normal concrete).

According to simulation results in Figure 5a, the failure mode for Conc1 show multiple shear band-type of failure planes which propagate mostly in the weaker outer product space. The failure mode predicted with Conc2, exhibit similar features but the failure planes are more vertical and resembles commonly observed axial splitting failure mode. In both cases, some unreacted cores have failed as well.
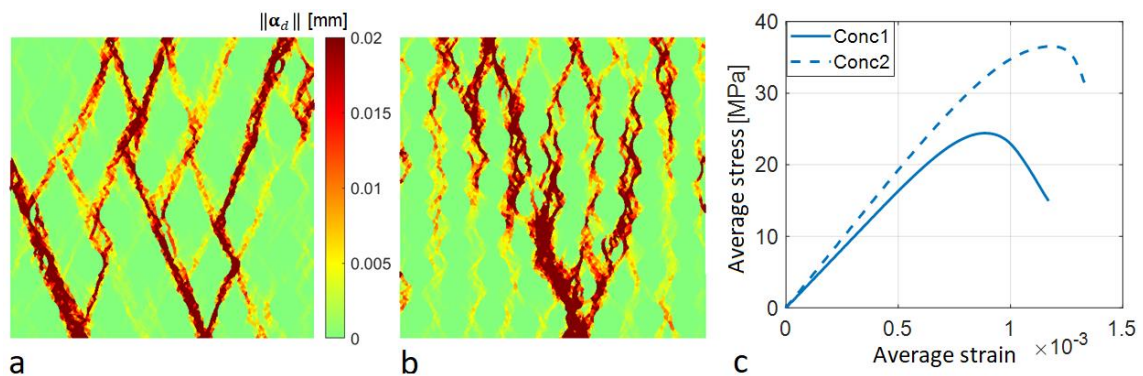

Figure 5. Simulation results for uniaxial compression test: Failure mode (in terms of crack opening magnitude) numerical concrete (Conc1) (a), numerical concrete 2 (Conc2) (b), and the corresponding stress-strain curves c).

As for the compressive strengths, being 24.4 MPa for Conc1 (higher w/c ratio) and 36.5 MPa for Conc2 (lower w/c ratio), the one with more water shows substantial weakening. However, comparison to experimental results is impossible as the exact w/c ratio of the numerical samples cannot be determined. The reason for the present model

62

predicting substantial weakening in compression but not in tension is as follows: First, it should be reminded that the failure of the cement particles and the inner products is by violation of the Rankine criterion, while the outer products can fail by shear and tension. Now, under tension, there is enough the weakest material, i.e., the outer products phase, in both samples for the tensile (mode I) failure to find its horizontal path through the specimen. However, this is not the case in compression, as can be observed in the failure modes in Figure 5, where the failure mode for Conc2, having the smaller amount of the weakest outer products phase (see Table 2), has a more vertical trend in the localized crack opening bands than the more inclined trend in the failure mode for Conc1. In other words, the smaller amount of the weakest phase forces the compressive fracturing to propagate in a less inclined manner, with respect to the loading axis, which naturally requires higher loading.

Finally, it is insightful to give a quantitative description of the effect of the w/c ratio on concrete strength. The classical Abrams relation [17] between the compressive strength and w/c ratio is

$$\sigma_c = A/B^{\frac{w}{c}} \tag{10}$$

where A and B are empirical constants depending on the cement type, aggregates, admixture, and age curing regimes. For the context of Abrams' tests, the constants A and B had values 14000 and 7, respectively, while the unit of compressive strength was psi. According to this law, when w/c ratio increases from 0.3 to 0.6, the compressive strength drops from 7809 psi (53.8 MPa) to 4355 psi (30 MPa).

Conclusions

The present numerical model based on embedded discontinuity finite elements correctly predicts the qualitative effect of water-to-cement ratio on the compressive strength of concrete, i.e., the higher the w/c ratio, the lower the concrete strength. However, the model does not predict the weakening effect for tensile strength due to the constant outer products phase strength assumption.

At the present preliminary stage of the model, only qualitative predictions are possible, as there is no link in the model between the w/c ratio and the distance of unreacted cement particle cores as well as the thickness of the inner reaction product layer. To make the model predictions quantitative, these parameters should be incorporated into the model, which is a nontrivial task. Moreover, the aggregates should also be included in further developments of the model. Finally, as the 2D plane strain assumption does not account for the true 3D geometry of the cement particles (or the aggregates), more reliable results could be obtained by a 3D extension of the present modelling approach.

Acknowledgements

References

[1] S.M. Levy. Construction Calculations Manual, Butterworth-Heinemann, 2012. https://doi.org/10.1016/C2009-0-64499-8

[2] J.G.M. van Mier. *Fracture processes of concrete: assessment of material parameters for fracture models*. Boca Raton, CRC Press, 1996.

[3] G. Hofstetter, G. Meschke (Eds.), *Numerical Modeling of Concrete Cracking*, CISM Courses and Lectures, vol. 532, Springer, 2011.

[4] A. Winnicki, C.J. Pearce, N. Bićanić. Viscoplastic Hoffman consistency model for concrete, *Computers & Structures*, 79:7–19, 2001. https://doi.org/10.1016/S0045-7949(00)00110-3

[5] P. Grassl, M. Jirásek. Damage-Plastic model for concrete failure. *International Journal of Solids and Structures*, 43:7166–7196, 2006. https://doi.org/10.1016/j.ijsolstr.2006.06.032

[6] P. Feenstra, R. De Borst. A composite plasticity model for concrete, *International Journal of Solids and Structures,* 33(5):707–30, 1996. https://doi.org/10.1016/0020-7683(95)00060-N

[7] E.N. Landis, J.E. Bolander. Explicit representation of physical processes in concrete fracture. *Journal of Physics D: Applied Physics,* 42:214002, 2009. https://doi.org/10.1088/0022-3727/42/21/214002

[8] P.E. Roelfstra, H. Sadouki, F.H. Wittmann. Le béton numérique. *Materials and Structures*, 18:327–335, 1985.

[9] A. Gangnant, J. Saliba, C. La Borderie, S. Morel. Modeling of the quasibrittle fracture of concrete at meso-scale: Effect of classes of aggregates on global and local behavior. *Cement and Concrete Research*, 89:35–44, 2016. https://doi.org/10.1016/j.cemconres.2016.07.010

[10] R.R. Pedersen, A. Simone, L.J. Sluys. Mesoscopic modeling and simulation of the dynamic tensile behavior of concrete. *Cement and Concrete Research*, 50:74–87, 2013. https://doi.org/10.1016/j.cemconres.2013.03.021

[11] T. Saksala. Numerical modelling of concrete fracture processes under dynamic loading: meso-mechanical approach based on embedded discontinuity finite elements. *Engineering Fracture Mechanics*, 201:282-297, 2018. https://doi.org/10.1016/j.engfracmech.2018.07.019

[12] S.M. Levy. Section 5 - Calculations Relating to Concrete and Masonry. In: S.M. Levy (Ed.), Construction Calculations Manual, Butterworth-Heinemann, 2012. https://doi.org/10.1016/C2009-0-64499-8

[13] J.C. Simo, J. Oliver, F. Armero. An analysis of strong discontinuities induced by strain-softening in rate-independent inelastic solids. *Computational Mechanics*, 12: 277–296, 1993. https://doi.org/10.1007/BF00372173

[14] J. Mosler. On advanced solution strategies to overcome locking effects in strong discontinuity approaches. *International Journal for Numerical Methods in Engineering*, 63:1313–1341, 2005. https://doi.org/10.1002/nme.1329

[15] R. Radulovic, O.T. Bruhns, J. Mosler. Effective 3D failure simulations by combining the advantages of embedded Strong Discontinuity Approaches and classical interface elements, *Engineering Fracture Mechanics*, 78: 2470–2485, 2011. https://doi.org/10.1016/j.engfracmech.2011.06.007

[16] W.M. Wang, L.J. Sluys, R. De Borst. Viscoplasticity for instabilities due to strain softening and strain-rate softening. *International Journal for Numerical Methods in Engineering,* 40: 3839–3864, 1997. https://doi.org/10.1002/(SICI)1097-0207(19971030)40:20<3839::AID-NME245>3.0.CO;2-6

[17] D.A. Abrams. Design of concrete mixtures. Bulletin 1, Structural Materials Research Laboratory, Lewis Institute, Chicago, USA, 1919.

Timo Saksala, Reijo Kouhia
Structural mechanics, BEN, Tampere University
P.O. Box 600, FI-33101 Tampere
timo.saksala@tuni.fi, reijo.kouhia@tuni.fi

Kari Kolari
VTT Technical Research Centre of Finland LTD
kari.kolari@vtt.fi